fluids

MDPI

Article

Probability-Based Droplet Modeling for In-Flight Icing Problems

Giulio Croce * and **Nicola Suzzi**

Polytechnic Department of Engineering and Architecture, University of Udine, 33100 Udine, Italy; nicola.suzzi@uniud.it
* Correspondence: giulio.croce@uniud.it

Abstract

A probability-based model (PBM) is developed to predict the evolution of a population of impinging droplets on a solid substrate and the eventual transition between dropwise and filmwise regimes. A dedicated heat transfer model is designed, in order to estimate the evaporating mass flux when the solid substrate is heated. Statistical information such as the droplet size distribution and the influence of surface wettability, required by the PBM, are derived using a previously developed high-fidelity individual-based model (IBM). The PBM is verified with the high-fidelity model for a small patch of solid substrate. Then, validation with experimental evidence from the literature is carried out in the case of in-flight ice on the NACA0012 airfoil. Results show that the present PBM is capable of investigating in-flight ice problems and can be integrated with a CFD analysis of the air flow past an airfoil flying through a cloud of supercooled droplets to predict the possible onset of ice accretion on the airfoil surface. Compared to Messinger-like models, the influence of surface morphology on runback water flow is incorporated in the PBM through the modeling of a discontinuous wetting layer, contributing to the design of passive and active anti-icing systems.

Keywords: in-flight icing; probability-based model; droplet impinging; surface wettability

1. Introduction

In the context of in-flight icing, an aircraft encounters a cloud of supercooled droplets, that may impact on the airfoil surface and eventually freeze instantaneously [1,2] (rime ice) or after the formation of rivulets and film (glaze ice). Ice accretion on the airfoil surface affects the aerodynamic performance in terms of lift, drag and stall onset. The problem is quite complex, coupling the solution of the flow field around the aircraft, the prediction of the droplet flow field and the resulting collection efficiency, and the simulation of the water layer evolution on the solid surfaces, including its phase changes. The source term in the mass balance, corresponding to the contribution of collection efficiency, can be estimated, using the CFD solution of the surrounding air flow field, via an Eulerian approach [3] or via a Lagrangian analysis [4,5], following the trajectories of the supercooled droplets in the surrounding air domain. Experimental campaigns and analytical models [6,7] address droplet rebound and splashing, which affect the effective collection efficiency [4]. With regard to the water layer simulation, existing in-flight ice models such as the commercial greensoftware FENSAP-ICE [8–10], the NASA-developed LEWICE and the non-open source ONICE3D successfully implement extended versions of the Messinger model [11–13], integrated with a CFD simulation of the flow past the airfoil. The Messinger model [11] assumes a continuous film layer driven by the shear, applied at the liquid–gas interface by the surrounding

Check for updates

Academic Editor: Xuemin Ye

Received: 4 April 2026
Revised: 19 May 2026
Accepted: 3 June 2026
Published: 7 June 2026

 https://doi.org/10.3390/fluids11060143

air flow, solving the mass and energy balances for the liquid phase to determine the liquid thickness and the freezing fraction. However, due to the continuous film assumption, the Messinger model cannot take into account the wettability of the airfoil surface, which may affect the actual liquid pattern. Indeed, passive anti-icing systems such as micro-structured superhydrophobic and ice-phobic surfaces not only promote the rebound of impinging droplets [4], but also maintain a discontinuous droplet pattern over the airfoil surface, which in turn yields a much faster liquid removal, if compared to a continuous film pattern. Hydrophobic and super-hydrophobic coatings are often presented in the literature as valuable tools for anti-icing feature enhancement: the mechanical stability, the corrosion resistance and the anti-ice properties of such superhydrophobic coatings on aluminium surface were evaluated in [14], while different ice-phobic coating and materials (including nano-textured lotus-leaf superhydrophobic surfaces, pitcher-plant slippery liquid-infused porous surfaces and soft materials with ultra-low ice adhesion strength) were tested in [15]; a hybrid superhydrophobic–superhydrophilic surface combined with an active anti-icing system was experimentally investigated in [16]. Recently, increasing attention has been devoted to droplet-based and wettability-aware icing models [17,18]. The effect of substrate wettability was incorporated into CFD ice accretion simulations in [17]. In that work, the collection efficiency, evaluated through a standard Eulerian framework, is corrected by a factor smaller than unity to account for splashing phenomena and the consequent mass loss of impinging droplets. Such a correction factor depends on both the local flow conditions and the substrate wettability. The evolution of the liquid layer over the solid surface is then modeled through lubrication theory (i.e., as a continuous thin film driven by shear stresses and local liquid-pressure gradients, similarly to Messinger-like models). Although the effects of a dropwise regime are partially included through the introduction of a wall slip boundary condition for superhydrophobic surfaces, lubrication theory inherently assumes the presence of a continuous wetting layer. Consequently, the detailed liquid distribution over the surface, as well as the possible transitions between continuous-film and discrete-droplet regimes, cannot be explicitly captured.

In order to overcome the inherent limitation of Messinger approach, the individual-based modeling (IBM) of the evolution of an impinging droplets population makes it possible to include the effect of surface wettability [4,19]. In [19], the history of each droplet is analyzed via a Lagrangian approach from the initial impinging on the solid surface to the final motion or disappearance due to evaporation (if an active anti-icing system is used), including coalescence with neighbour drops and growth induced by impinging of tiny droplets from the clouds. The departure radius and the eventual droplet velocity are affected by the substrate wettability (i.e., by the static, advancing and receding contact angles) [20,21] as well as the evaporation rate [22–24]. Unfortunately, since the in-flight ice problem is inherently multiscale (from the micrometer size of the impinging droplets to the multi meters scale of the whole aircraft flow field), such a detailed modeling is not suitable to be coupled with a fully CFD analysis of the surrounding air flow, due to the unaffordable computational cost. However, the numerical analysis via high-fidelity IBMs represents a valuable tool to understand the physics driving the in-flight ice phenomenon, since experimental campaigns are quite difficult due to both the interaction between droplets and macro-scale flow field and the measurement challenges. Furthermore, IBMs provide statistical information, required to develop a reliable probability-based model (PBM), which entails negligible computational effort compared to IBMs while capturing the effects of the dropwise regime on the runback water flow and on the onset of icing, overcoming the limitations of the classical shear-driven film assumption typically adopted by Messinger-like models. The statistical droplet size distribution, which was obtained through post-processing of IBM computations in [19], represents, together with the modeling of moving droplet dynamics and heat and mass transfer process, the core of the PBM; the growth timescale of a stationary droplet from its impingement on the solid surface to its motion due to combined coalescence and impinging processes, numerically computed in [19] via IBM under different flow conditions, is used to predict the icing onset when passive anti-icing systems are used. Such an approach is widely used to model dropwise condensation of vapor steam or humid air [25–27], but its application to in-flight ice is still limited, with a first attempt to develop a dedicated PBM presented in [4].

Here, a novel PBM is developed to analyze correctly the water layer under the dropwise regime induced by superhydrophobic coatings: the mass balance is solved for the liquid layer evolving on the airfoil surface; compared to a standard Messinger model, the influence of the effective liquid pattern (filmwise or dropwise) is included in the calculation of both the runback liquid flow and the wet fraction. The statistical droplet size distribution, required by the PBM, was derived in [19] from the high-fidelity numerical simulations. Such information is used by the novel PBM to determine the wet fraction of solid substrate and the radius of the largest droplet from the amount of impinged liquid: the former allows the prediction of transitions between droplet regime and continuous film, while the latter is compared with the departure radius to assess whether a liquid flow develops. In order to estimate the runback water flow in the dropwise regime, dedicated models for the departure radius and for the velocity of moving droplets are included in the PBM. The energy balance is solved to estimate the evaporating flow rate, if an active anti-icing system is used. The growth timescale of a stationary droplet from its impingement is here correlated to its radius using data provided by the IBM computation. The comparison of the growth timescale of a stationary droplet with the freezing time provides a criterion to evaluate the onset of icing when passive anti-icing systems are adopted. However, the details of the subsequent ice accretion process are beyond the scope of the present PBM, which is aimed at providing the information required by ice accretion models integrated into CFD solvers to predict ice growth. The PBM is firstly compared with the high-fidelity individual-based model (IBM), previously developed and validated [19], in order to test its capability to predict the liquid layer evolution on a small patch of solid surface under different operating conditions. Assuming an adiabatic airfoil surface, the PBM is then compared with a standard film model, which assumes a continuous film pattern, in order to highlight the differences in the predicted liquid thickness. A qualitative validation against experimental icing data available in the literature [16] is performed for the case of the impinging of supercooled droplets on an NACA0012 airfoil, whose surface is partially heated, with different coating solutions being investigated.

2. Materials and Methods

2.1. Probability-Based Model

In order to predict the liquid layer evolution on a solid surface, the mass balance, which includes the net liquid flux crossing the solid surface boundaries, the source term due to impinging of liquid droplets from the clouds, the evaporating/freezing mass fluxes, is numerically solved. Thus, the mass balance on a control element of solid substrate yields

$$\frac{\mathrm{d}m_l}{\mathrm{d}t} = \xi \, LWC \, u_\infty \, S - \left(\dot{m}''_{lv} + \dot{m}''_{ls} \right) S - \int_{\partial S} \rho_l \, \mathbf{q} \cdot \hat{\mathbf{n}} \, \mathrm{d}s \tag{1}$$

where S and ∂S are the area and the perimeter of the control element, m_l is the liquid mass inside the control element, ξ is the collection efficiency (i.e., the fraction of the freestream incoming droplets locally impinging on the airfoil surface), LWC is the liquid water content, $\dot{m}''_{lv}$ is the evaporating mass flux ($\dot{m}''_{lv} > 0$ if an active anti-icing system is used) and $\dot{m}''_{ls}$ is the freezing mass flux, $\mathbf{q}$ is the liquid volumetric flux per unit length crossing ∂S and $\hat{\mathbf{n}}$ is the outward normal direction to ∂S.

In order to numerically solve Equation (1) on a discretized solid surface, the liquid flux crossing the mesh element boundaries must be estimated as a function of the liquid mass in the control element. Assuming that the liquid pattern evolves as a population of droplets, that can grow due to impinging and coalescence and eventually move due to the drag force of the surrounding air flow, the average liquid thickness and the wet fraction can be expressed as

$$h = \frac{m_l}{\rho_l\, S} = \int_{r_0}^{r_{max}} n_r\, V_d\, \mathrm{d}r \tag{2}$$

$$\eta = \frac{S_{wet}}{S} = \int_{r_0}^{r_{max}} n_r\, S_b\, \mathrm{d}r \tag{3}$$

where r_0 is the radius of a newly impinged droplet, r_{max} is the radius of the largest droplet, n_r is the droplet size distribution, V_d is the droplet volume and S_b is the droplet base area. The radius r_0 of a newly impinged droplet, which corresponds to the minimum radius of the droplets population, is correlated to the impinging radius before impact on the solid surface and to the static contact angle [19]:

$$r_0 = r_{imp} \left(\frac{4}{2 - 3\,\cos\theta_s + \cos^3\theta_s} \right)^{1/3} \tag{4}$$

The volume and the base area of a droplet having radius r are estimated assuming a spherical cap with prescribed contact angle equal to the static value:

$$V_d = \frac{\pi}{3}\, r^3 \left(2 - 3\,\cos\theta_s + \cos^3\theta_s\right),\; S_b = \pi\,(r\,\sin\theta_s)^2 \tag{5}$$

In order to apply Equations (2) and (3), the statistical droplet size distribution n_r is required. Since such information cannot be derived theoretically, it must be obtained either from experimental data or through post-processing of IBM simulations. It was proved in [19] that the size distribution of an impinging droplet population can be estimated using the Le Fevre and Rose correlation [28],

$$n_r = \frac{1}{3\,\pi\, r_{mov}\, r^2} \left(\frac{r_{mov}}{r}\right)^{2/3} \tag{6}$$

with r_{mov} being the departure radius. Therefore, the correlation $n_r(r)$ for the droplet size distribution requires only the departure radius, which is affected by the local air flow conditions and by the surface wettability, as discussed in Section 2.2.

Substituting the droplet size distribution in Equations (2) and (3) yields the following:

$$h = \frac{{r_{max}}^{4/3} - {r_0}^{4/3}}{12\, {r_{mov}}^{1/3}} \left(2 - 3\,\cos\theta_s + \cos^3\theta_s\right) \tag{7}$$

$$\eta = \frac{{r_{max}}^{1/3} - {r_0}^{1/3}}{{r_{mov}}^{1/3}}\, \sin^2\theta_s \tag{8}$$

The wet fraction offers a rough way to predict the flow pattern: a droplet regime is expected when $\eta < 1$, while a continuous film is expected when $\eta \geq 1$.

If $\eta < 1$ and $r_{max} > r_{mov}$, the liquid flux, due to the moving droplets, is estimated as

$$q = \int_{r_{mov}}^{r_{max}} n_r\, V_d\, u_d\, \mathrm{d}r \tag{9}$$

https://doi.org/10.3390/fluids11060143

with u_d being the droplet velocity. When solving the mass balance over a solid surface, the local value of the maximum droplet radius r_{max} must first be estimated from the average liquid thickness, $h = m_l/(\rho_l\, S)$, using Equation (7). Once r_{max} is known, the wet fraction η is estimated using Equation (8) and the local liquid pattern is then predicted based on the computed value of η: if a droplet regime is predicted (i.e., $\eta < 1$), the liquid flux q is estimated via Equation (9) when r_{max} exceeds the departure radius r_{mov}; if a continuous liquid layer is predicted, a standard shear-driven film model is considered instead. It is worth noting that Equation (9), which provides the local liquid flux, relies on the statistical droplet size distribution, Equation (6), and on the modeling of moving droplet dynamics.

2.2. Droplet Motion

Following [19], the departure radius and the droplet velocity are estimated via the solution of the force and energy balances for a droplet subjected to drag and surface tension:

$$r_{mov} = \frac{96}{\pi^3}\,\frac{\sigma_{lv}\,\sin\theta_s}{\rho_g\, c_D\, {u_g}^2}\,\frac{\cos\theta_r - \cos\theta_a}{\theta_s - \sin\theta_s\,\cos\theta_s} \tag{10}$$

$$\frac{u_d}{u_g} = 1 + \chi - \sqrt{(1+\chi)^2 - \left(1 - \frac{r_{mov}}{r}\right)} \tag{11}$$

$$\chi = \frac{\pi\,\mu_l}{3\,\rho_g\, c_D\, u_g\, r}\,\frac{2 + \cos\theta_s + 6\,\sin\theta_s\, c_\theta\,\log(r/l_{sca})}{\theta_s - \sin\theta_s\,\cos\theta_s} \tag{12}$$

with u_g being the local air velocity, $l_{sca} = 10^{-7}$ m being the scaling length for wedge viscous dissipation, $c_D = 9\times10^{-2}$ being the drag coefficient of a flow past a protuberance on a flat substrate and c_θ being a function of the static contact angle [20]. Applying a wall function to approximate the flow field yields the estimate of the local gas velocity u_g at a distance $r\,(1-\cos\theta_s)$ from the solid substrate. Since u_g depends on the droplet radius, the solution of Equation (10) is iterated until convergence of r_{mov} is achieved.

2.3. Droplet Growth Timescale

In order to predict the ice accretion, it must be determined whether a droplet freezes or not. Thus, given a droplet of radius r, its age (i.e., the time-lapse between impinging and growth up to the actual size r) must be estimated and compared with the freezing time of the droplet bead, the latter depending on the liquid subcooling. Knowing the number of impinging drops (assumed as spheres of radius r_{imp}) falling on the top surface of a droplet already stuck to the solid substrate, $\mathrm{d}N_{imp} = J_{imp}\,\pi\,(r + r_{imp})^2\,\mathrm{d}t$, its growth rate due to impinging process is equal to

$$G = \frac{\mathrm{d}r}{\mathrm{d}t} = \frac{4\,\pi\, J_{imp}\, {r_{imp}}^3}{3\,(2 - 3\,\cos\theta_s + \cos^3\theta_s)}\left(\frac{r + r_{imp}}{r}\right)^2,\quad J_{imp} = \frac{3\,\xi\, LWC\, u_\infty}{4\,\pi\,\rho_l\, {r_{imp}}^3} \tag{13}$$

where J_{imp} is the impinging rate, i.e., the number of droplets impacting the solid per unit surface area and unit time.

The mean droplet age is derived from the growth rate induced by impinging via integration over time:

$$\tau(r) = \int_{r_0}^{r}\frac{\mathrm{d}r}{G} = \tau_0\left[\frac{r - r_0}{r_0}\left(1 + \frac{{r_{imp}}^2}{(r + r_{imp})\,(r_0 + r_{imp})}\right) - 2\,\frac{r_{imp}}{r_0}\,\log\left(\frac{r + r_{imp}}{r_0 + r_{imp}}\right)\right] \tag{14}$$

$$\tau_0 = \left(\frac{4}{3}\,\pi\, {r_0}^2\, J_{imp}\right)^{-1} \tag{15}$$

Given a stationary droplet of radius $r < r_{mov}$, if the time-lapse $\tau(r)$ since its impingement exceeds the freezing onset τ_{ice}, an ice bead forms. The mass of freezing droplets per unit time yields the icing mass flux $\dot{m}''_{ls}$.

2.4. Heat Transfer Model

A proper heat transfer modeling is required to evaluate the evaporating mass flux $\dot{m}''_{lv}$ in Equation (1) when an active anti-icing system is used. A standard Messinger model can be used to predict the heat and mass transfer rate for a continuous film pattern. On the other hand, if a droplet regime is detected, i.e., $\eta < 1$, the heat transfer model must include the discontinuous liquid distribution over the solid substrate to ensure accurate predictions. Following [23], the evaporating flow rate through the free surface of an isolated droplet of radius r on a solid surface assuming vapor diffusion can be estimated as

$$\dot{m}_{d,0} = \pi \, \sin\theta_s \, f_\theta \, r \, D_v \, (\rho_{v,s} - \rho_{v,\infty}) \tag{16}$$

$$\rho_{v,s} = \frac{p_{sat}(T_s)}{R_v \, T_s}, \; \rho_{v,\infty} = \frac{\phi \, p_{sat}(T_\infty)}{R_v \, T_\infty} \tag{17}$$

where T_s is the solid surface temperature, D_v is the diffusion coefficient of vapor in air, ϕ is the relative humidity of the surrounding air flow, f_θ is a coefficient depending on the static contact angle [23] and p_{sat} denotes the saturation pressure. Since the surrounding air flow is characterized by high undisturbed velocity typical of in-flight ice application, the effect of vapor convection, which enhances mass transfer, is included using the heat and mass transfer analogy. Following [29], the effective evaporating flow rate is evaluated using the heat and mass transfer analogy,

$$\dot{m}_d = \mathrm{Sh} \, \dot{m}_{d,0}, \; \mathrm{Sh} = \mathrm{Nu} \left(\frac{\mathrm{Sc}}{\mathrm{Pr}} \right)^{1/3} \tag{18}$$

where $\mathrm{Sh} = k_v \, l_c / D_v$ is the Sherwood number, $\mathrm{Nu} = \alpha \, l_c / \lambda_g$ is the Nusselt number, $\mathrm{Sc}/\mathrm{Pr} \simeq 1$ for air, and k_v and α are the mass transfer coefficient and the convection coefficient. The global evaporating mass flux, which includes the contributions of each droplet, is estimated from the known drop size distribution:

$$\dot{m}''_{lv} = \int_{r_0}^{r_{max}} n_r \, \dot{m}_d \, \mathrm{d}r \tag{19}$$

Since the Le Fevre & Rose correlation, Equation (6) is valid for $r \geq r_0$ [19], the contribution from evaporation of small droplets (characterized by $r \leq r_0$) is neglected. However, it was demonstrated in [19] that the contribution of small droplets to the latent heat flux is less than 10%.

3. Results and Discussion

3.1. Model Verification

The PBM is firstly verified with the high-fidelity Lagrangian code, previously implemented in `FORTRAN` and validated in [19]. We refer to [19] for the detailed description of the mathematical model and implemented algorithm. Consistently with in-flight icing applications, the undisturbed flow velocity is set to $u_\infty = 100\,\mathrm{m/s}$, and the liquid water content and the impinging radius are set to the reasonable values of $LWC = 4\,\mathrm{g_l/m^3}$ and $r_{imp} = 10^{-2}\,\mathrm{mm}$. The local collection efficiency and the local skin-friction coefficient are set to $\xi = 10^{-1}$ and $c_f = 10^{-3}$. A hydrophobic substrate characterized by receding contact angle equal to $\theta_r = 100°$, and advancing contact angle $\theta_a = 140°$ is considered. The static contact angle is derived as follows:

$$\theta_s = \arccos\left(\frac{\cos\theta_r + \cos\theta_a}{2}\right) \tag{20}$$

Both the liquid and the air properties are evaluated at $p_\infty = 101,325\,\text{Pa}$, $T_\infty = 0\,°\text{C}$. The corresponding departure radius is $r_{mov} = 0.341\,\text{mm}$. An adiabatic solid substrate is assumed (i.e., $\dot{m}''_{lv} = 0$). Since the aim is to compare the liquid layer evolution from the Lagrangian simulation with that predicted by the PBM, icing is suppressed (i.e., $\dot{m}''_{ls} = 0$). A small patch of $S = 7.5 \times 3\,\text{mm}^2$ is investigated using the high-fidelity code, while the PBM is solved on a single control surface having the same size. In order to perform time integration of Equation (1), the actual liquid mass m_l is used to predict the radius of the largest droplet via Equation (2); when $r_{max} > r_{mov}$, the volumetric liquid flux q is evaluated via Equation (9); the Le Fevre and Rose correlation provides the required statistical drop size distribution.

The time integration step for both the Lagrangian computation and the PBM is set to $\Delta t = 1.25 \times 10^{-2}\,\text{s}$. In order to generalize the problem, it is useful to scale the numerical results using the radius of a newly impinged droplet and the time required to fill the domain with a population of equally spaced droplets of radius r_0,

$$t_0 = \left(4\, J_{imp}\, {r_0}^2\right)^{-1} \tag{21}$$

with J_{imp} being the impinging rate. Scaling by r_0 and t_0, the only problem parameters are: the normalized departure radius r_{mov}/r_0; the static contact angle θ_s; the non-dimensional parameter $\chi(r_{mov})$, correlated to the ratio between drag force and viscous force acting on a moving droplet. Figure 1 depicts the evolution of the droplet population at successive instants: two large droplets move downward along the vertical axis driven by shear and are subsequently shed from the surface at $t = 62.4\,\text{s}$ and $t = 62.8\,\text{s}$, coalescing with the droplets along the moving path and leaving a dry trace aligned with the vertical axis, subsequently filled by small newly impinged droplets; then, another sweeping event is observed at $t = 63.4\,\text{s}$, after a group of three droplets coalesce into a large drop with $r > r_{mov}$, triggering droplet motion.

The mean liquid thickness h and the wet fraction η predicted by the PBM (Equations (7) and (8)) are compared with those coming from the high-fidelity computations in Figure 2a,b, showing a good agreement. Indeed, the steady state solution for h and η predicted by the PBM is equal to the time-averaged values of the Lagrangian computations, characterized by a self-similar behavior due to the sequence of wetting and dewetting cycles. Since both the number and the size of moving droplets leaving the computational domain are characterized by a large scattering, the time-averaged liquid flux, $\overline{q}(t) = \sum_{i=1}^{n_t} q\,\Delta t/t$, is determined via post-processing of numerical data and compared with the PBM in Figure 2c: a discrepancy of about 11% is observed for $t/t_0 > 160$.

Further computations were run using the high-fidelity Lagrangian code, in order to check the consistency of Equations (6) and (14), used to predict the drop size distribution and the droplet age in the PBM, at different values of the normalized departure radius r_{mov}/r_0. Thus, the undisturbed air flow velocity was set to $u_\infty = 50, 100$ and $150\,\text{m/s}$, while the same substrate wettability, liquid water content, collection efficiency and skin-drag coefficients are assumed: $LWC = 4\,\text{g/m}^3$, $\xi = 10^{-1}$, $c_f = 10^{-3}$. A $7.5 \times 3\,\text{mm}^2$ computational domain was considered for $u_\infty = 100$, $150\,\text{m/s}$ (yielding $r_{mov} = 0.167$, $0.341\,\text{mm}$), while a $7.5 \times 5\,\text{mm}^2$ domain was investigated for $u_\infty = 50\,\text{m/s}$ (corresponding to $r_{mov} = 1.663\,\text{mm}$). The time integration step was set to $\Delta t = 5 \times 10^{-2}\, t_0$.

https://doi.org/10.3390/fluids11060143

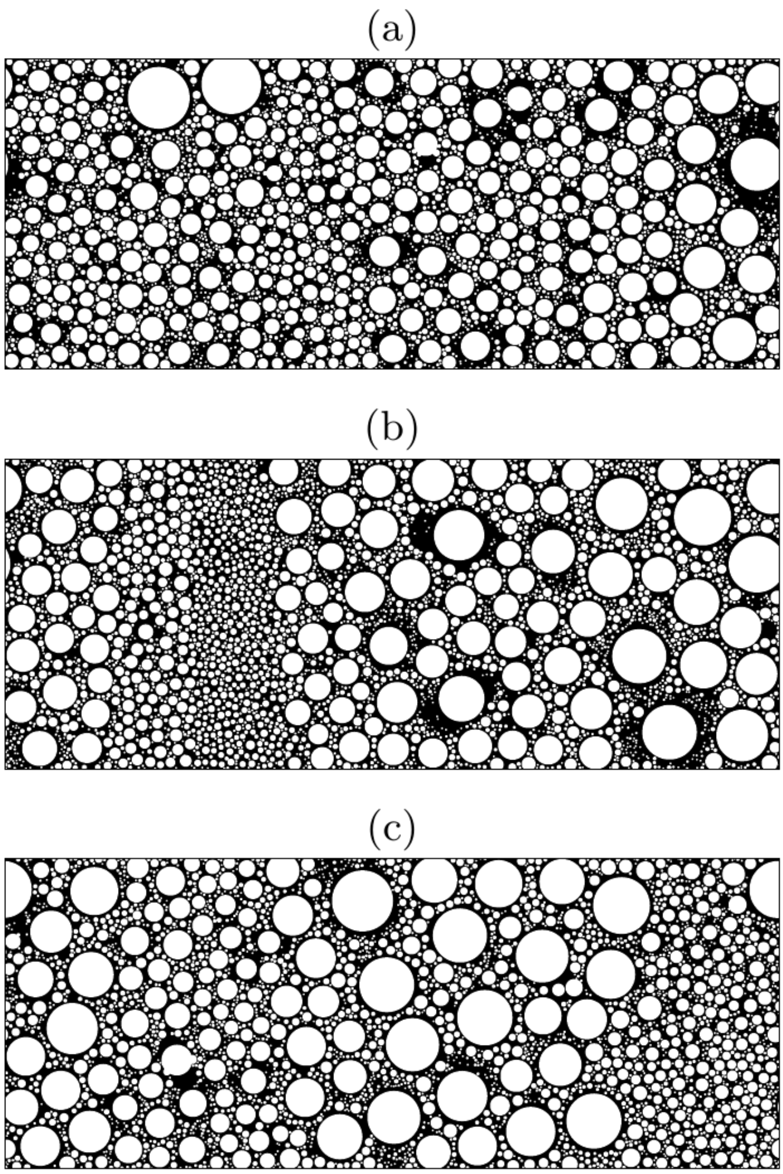

Figure 1. Droplet population at successive instants: (**a**) $t = 61.8\,\mathrm{s}$; (**b**) $t = 63\,\mathrm{s}$; (**c**) $t = 64.2\,\mathrm{s}$. $7.5 \times 3\,\mathrm{mm}^2$.

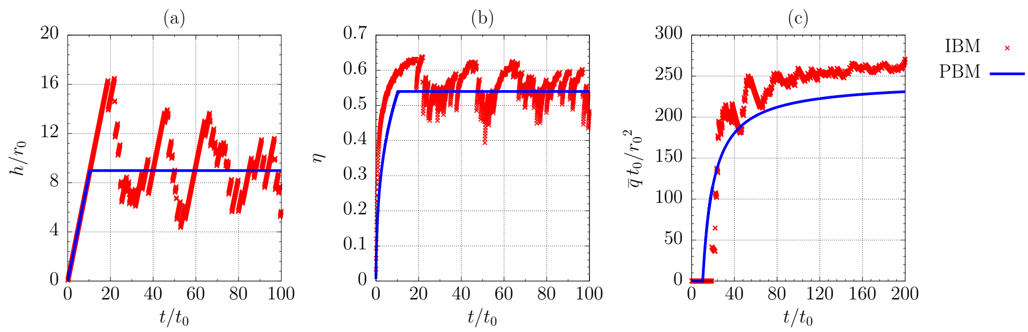

Figure 2. Comparison between probability-based model and high-fidelity Lagrangian code: (**a**) average liquid thickness versus time; (**b**) wet fraction versus time; (**c**) time-averaged volumetric flux leaving the computational domain.

Figure 3 compares the Le Fevre and Rose correlation, Equation (6), with the numerical drop size distribution from the Lagrangian computations. A great agreement is observed for all the investigated air flow velocities u_∞, corresponding to departure radii r_{mov}/r_{imp}

in the typical in-flight icing applications range 10^1–10^2. The mean droplet age $\tau(r)$ from numerical computations is also compared with that predicted by Equation (14) in Figure 4: a good agreement is observed for the large droplets, having $r/r_0 \geq 10$; according to Equation (14), $\tau(r)$ is slightly affected by the departure radius. Since the freezing onset is based on the age of the oldest, still droplet, which corresponds to $\tau(r_{mov})$, we may be confident in using Equation (14).

It is worth pointing out that the IBM computations, run using an in-house code implemented in FORTRAN and parallelized for a shared-memory machine using OpenMP, required about 2 h each on an 8-core, 32 GB memory workstation, while the PBM is essentially instantaneous, making it well suited to be integrated in CFD frameworks as a solid-flow interface for in-flight icing simulations.

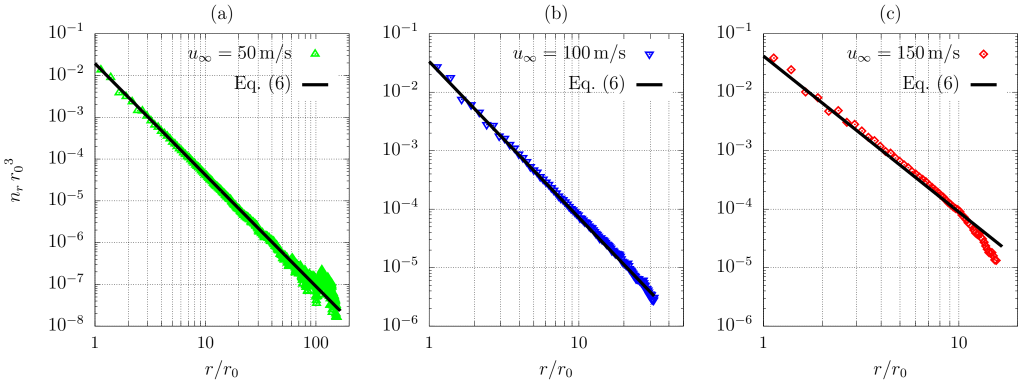

Figure 3. Numerical droplet size distribution versus Le Fevre and Rose correlation, Equation (6): (**a**) $u_\infty = 50\,\mathrm{m/s}$; (**b**) $u_\infty = 100\,\mathrm{m/s}$; (**c**) $u_\infty = 150\,\mathrm{m/s}$.

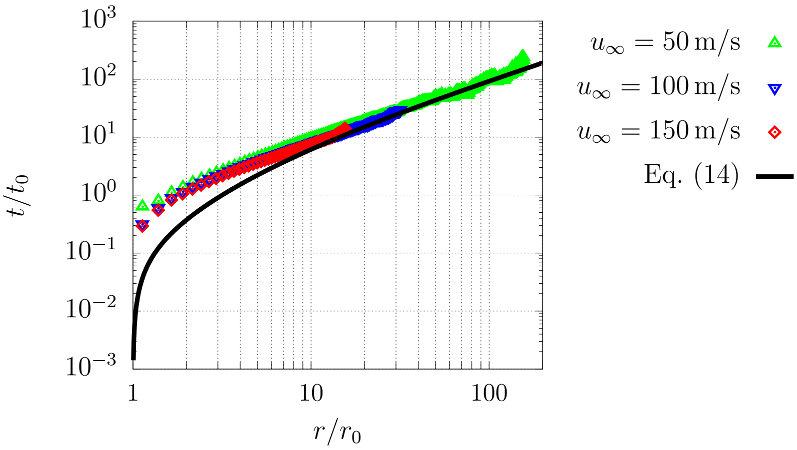

Figure 4. Mean droplet age: numerical results from IBM versus correlation, Equation (14).

3.2. Pbm Versus Shear-Driven Film Model

The impinging of liquid droplets over NACA0012 airfoil is investigated. The same test case as [16], reported in Table 1, is considered: tiny liquid droplets having diameter in the range 10–100 µm are injected in air flowing with undisturbed velocity of $u_\infty = 40\,\mathrm{m/s}$ past an NACA0012 airfoil having chord length of $l_c = 150\,\mathrm{mm}$. Since the PBM is specifically aimed at describing the evolution of the liquid layer, icing is intentionally suppressed by considering an environmental temperature of $T = 0\,°\mathrm{C}$: this configuration enables a direct comparison between the liquid-layer dynamics predicted by the present PBM and those obtained with a standard shear-driven film model, which is the basis of Messinger-like models; the effect of surface wettability on the onset of icing will be discussed later. Properties of liquid water are evaluated at $p_\infty = 101{,}325\,\mathrm{Pa}$, $T_\infty = 0\,°\mathrm{C}$; the NACA0012 airfoil surface is assumed adiabatic (i.e., no active anti-icing system is applied); the wettability of the superhydrophobic coating used in [30] is investigated.

Table 1. Impinging over NACA0012 airfoil: investigated test case.

Air Flow Conditions		**Superhydrophobic**	
u_∞ (m/s)	40	θ_a (deg)	159
T_∞ (°C)	−5	θ_r (deg)	154
l_c (mm)	150	θ_s (deg)	157
AoA (deg)	0		
LWC (g/m^3)	1		
d_{imp} (µm)	10–100		

In order to estimate both the skin-friction coefficient and the collection efficiency along the airfoil profile, the air flow field past NACA0012 is solved using the open source SU2 solver. The computed flow field is used for the Lagrangian tracking of the droplets eventually impinging on the airfoil. Following [4], the trajectories of an array of N_d droplets of radius r_{imp}, initialized through a vertical section far from the airfoil leading edge, are traced. At each time step, the force balance is solved for each droplet. Assuming that gravity force can be neglected [4], drag forces drive the motion of the impinging drops,

$$\frac{4}{3}\rho_l\,\pi\,r_{imp}{}^3\,\frac{\mathrm{d}\mathbf{u}}{\mathrm{d}t} = \frac{1}{2}\rho_a\,c_D\,\left(\mathbf{u_g}-\mathbf{u}\right)\left|\mathbf{u_g}-\mathbf{u}\right| \tag{22}$$

where the local air velocity u_g is evaluated interpolating the flow field solution, while the drag coefficient c_d is estimated as that of a flow past a sphere [31]. The droplet position is updated at each time step. Whether a droplet impacts the airfoil surface, it is assumed that the droplet sticks on it. The collection efficiency is, thus, derived from the number of droplets impacting the airfoil per unit surface.

The computed collection efficiency along the airfoil profile is shown in Figure 5a for different values of the impinging radius, while the skin-friction coefficient, derived from SU2 computation at $\mathrm{Re}_\infty = \rho_g\,u_\infty\,l_c/\mu_g = 4.5\times10^5$ and required to estimate the departure radius and the velocity of moving droplets, is given in Figure 5b. The PBM solution is compared with a standard shear-driven film model, which assumes a continuous film wetting the airfoil surface and is the basis of Messinger-like models typically used to predict ice accretion. Thus, Equation (1) is numerically solved: when a dropwise regime is assumed, the liquid flux is estimated via Equation (9), as described in Section 2.1; when a continuous wetting layer is assumed, the liquid flux is estimated as follows:

$$q = \frac{1}{2}\,\frac{\tau_{lg}}{\mu_l}\,h^2,\;\; \tau_{lg} = \frac{1}{2}\,\rho_g\,c_f\,u_\infty{}^2 \tag{23}$$

Since an adiabatic airfoil profile is assumed (i.e., no anti-icing system is used), the evaporating mass flux in Equation (1) is set to zero, $\dot{m}''_{lv} = 0$. The airfoil profile is discretized via a 1D mesh of 1664 elements with a spatial discretization step equal to $2\times10^{-4}\,l_c$ close to the leading edge. A first-order upwind scheme is implemented to compute the liquid fluxes through the element faces, while time marching is performed via an explicit forward Euler scheme, until a steady state condition is reached.

Figure 6a shows the computed liquid layer profiles along the chordwise coordinate, predicted by the PBM and by a standard shear-driven film model: a large discrepancy is observed close to the leading edge, with a thicker liquid layer predicted by the PBM, due to the locally large departure radius; on the other hand, the dropwise regime predicts a thinner average liquid thickness where the departure radius reach its smallest value (corresponding to large values of the skin-friction factor). It is worth pointing out that the average liquid thickness predicted by the PBM is affected by the surface wettability: hydrophilic surfaces, usually characterized by large contact angle hysteresis, yields a thicker liquid layer, compared to the superhydrophobic surface here considered. Figure 6b depicts the local value of the maximum droplet radius (i.e., the size of the largest droplet, which has to be higher than the departure radius in order to have a runback liquid flow) and the wet fraction of solid surface along the airfoil profile. The wet fraction, which is used to roughly predict the transition between dropwise and filmwise regimes, is an important parameter since it also gives information about the eventual ice shape.

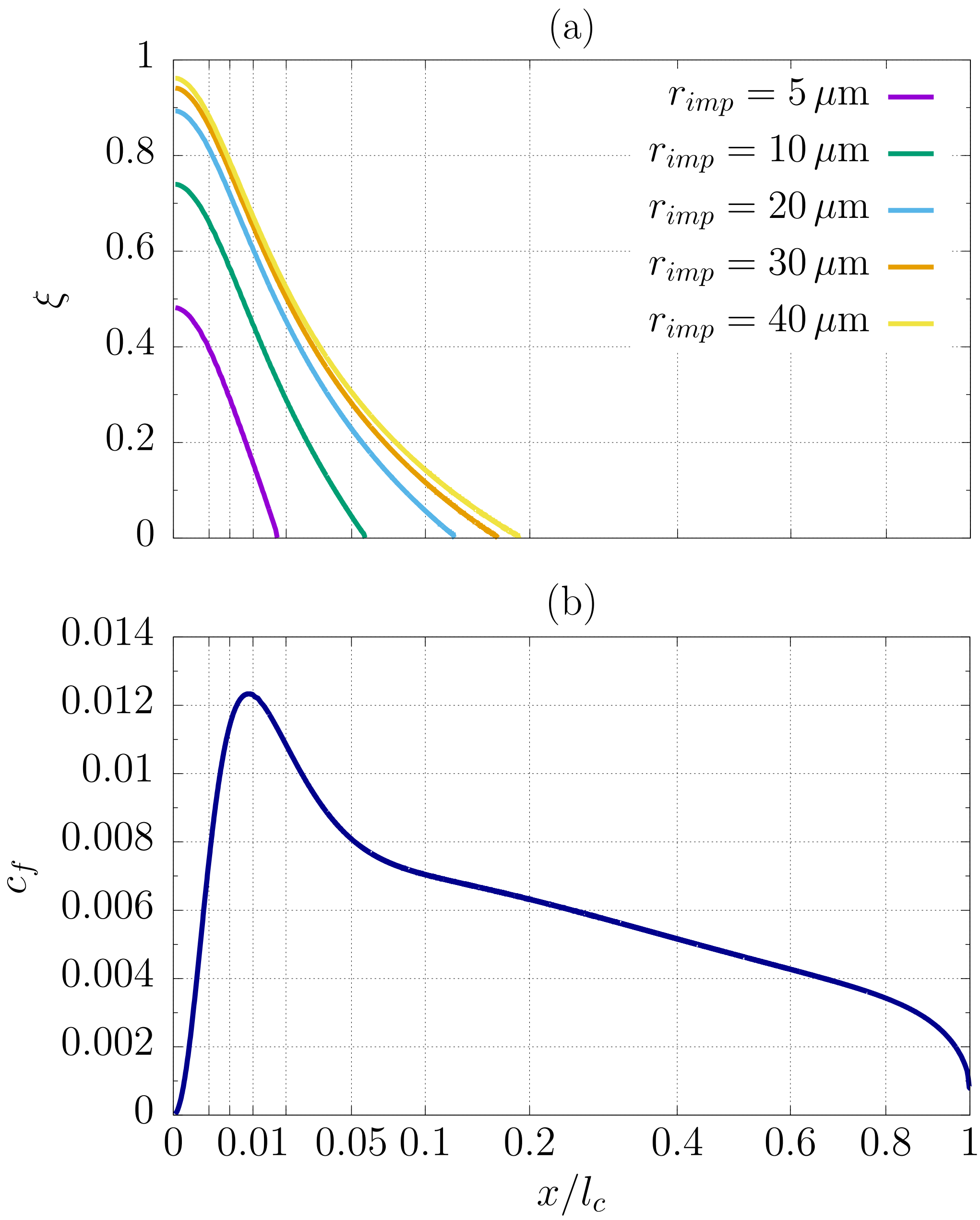

Figure 5. (**a**) Collection efficiency η at different impinging radii. (**b**) Skin-friction coefficient along NACA0012 profile for $\mathrm{Re}_\infty = 4.5 \times 10^5$, AoA $= 0°$. Chordwise coordinate scaled as $\sqrt{x/l_c}$, $u_\infty = 40\,\mathrm{m/s}$, $l_c = 150\,\mathrm{mm}$.

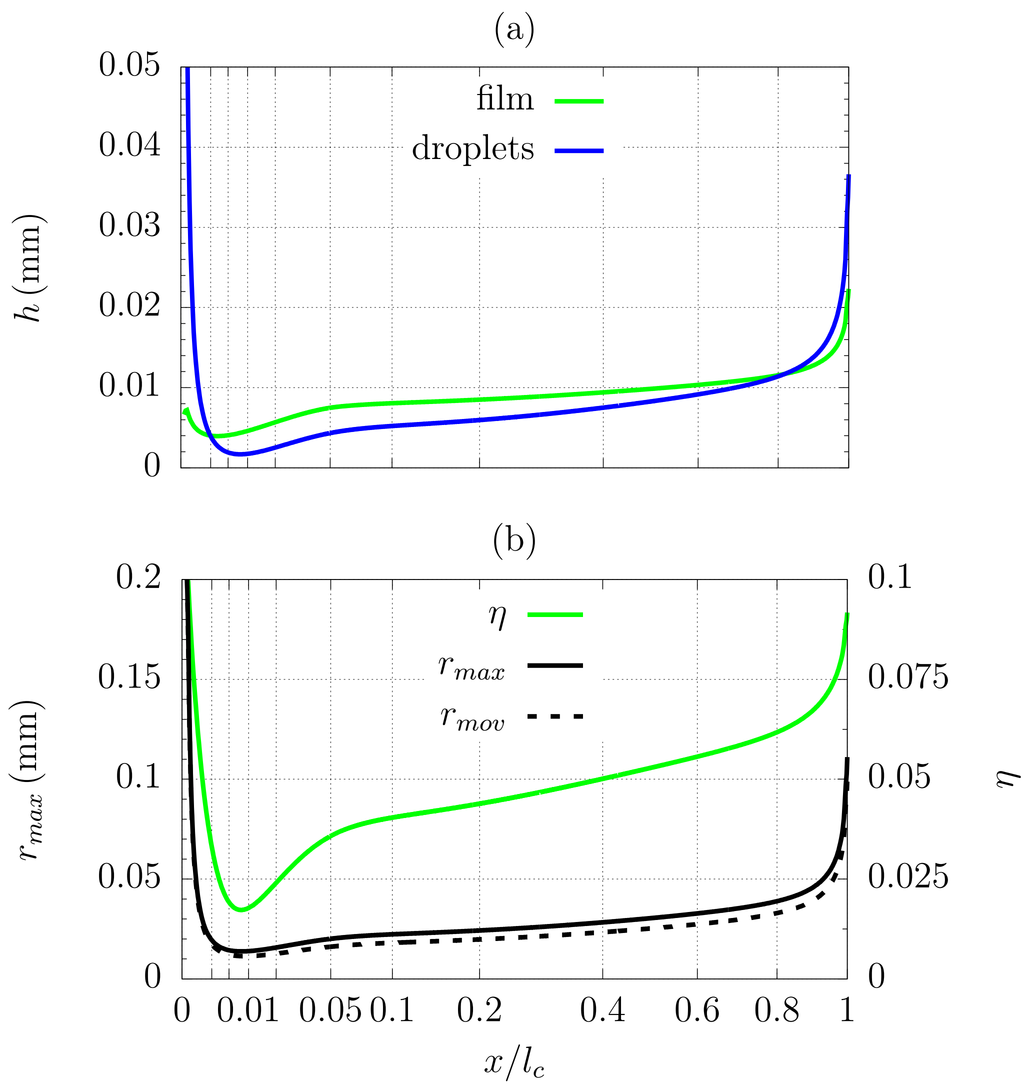

Figure 6. (**a**) Liquid layer thickness along chordwise coordinate: PBM (blue line) vs. shear-driven film model (green line). (**b**) Maximum droplet radius r_{max} (black solid line), departure radius r_{mov} (black dashed line) and wet fraction η (green solid line) predicted by PBM along chordwise coordinate. $r_{imp} = 10\,\mu\text{m}$, $l_c = 150\,\text{mm}$, $LWC = 1\,\text{g/m}^3$, $u_\infty = 40\,\text{m/s}$.

3.3. Validation of the PBM

The PBM is qualitatively validated with the experimental evidence of [16] when an active anti-icing system is used. The test case of Table 1 is considered: tiny droplets with $d_{imp} = 10\,\mu\text{m}$ are injected in saturated moist air at $T_\infty = -5\,^\circ\text{C}$ flowing with undisturbed velocity $u_\infty = 40\,\text{m/s}$ past an $l_c = 150\,\text{mm}$ NACA0012 airfoil. Following [16], a portion corresponding to 5% of the chord length is heated. Since the imposed impinging diameter is equal to $d_{imp} = 10\,\mu\text{m}$, which falls in the range experimentally observed in [16], the whole portion of airfoil surface subjected to impinging (about 2% of the chord) is included in the heated section. In order to validate the PBM against the experimental observations reported in [16] and to compare numerical results with those of a standard Messinger model, the onset of icing is included in the modelling framework: the number of freezing droplets per unit surface, which yields the freezing flux $\dot{m}''_{lv}$, is determined following the procedure described in Section 2.3.

A specific heat flux of $\dot{Q}''_s = 13\,\text{kW/m}^2$, which falls in the range of in-flight icing application, is imposed through the heated portion of the solid surface. Since the heat transfer model requires the local substrate temperature T_s, the following energy balance is solved to evaluate T_s inside the heated section of length $l_h = 0.05\, l_c$,

$$\dot{Q}_s'' = \alpha\, (T_s - T_\infty) + \dot{m}_{lv}''\, h_{lv} \tag{24}$$

with $\dot{m}_{lv}''$ being evaluated as a function of T_s via Equation (19). Since $\dot{m}_{lv}''$ depends on T_s, its value is iteratively updated until Equation (24) is verified. The local heat transfer coefficient α over the NACA0012 airfoil is estimated via SU2. The solid substrate is assumed to be adiabatic outside the heated section. If a liquid flow rate per unit airfoil width q exits the heated section, an energy balance is solved to estimate the local liquid temperature T_l downstream of the heated section,

$$q\, c_{pl}\, \frac{\mathrm{d}T_l}{\mathrm{d}s} = \alpha\, \eta\, (T_l - T_\infty), \;\; T_l|_{x=l_h} = T_s|_{x=l_h} \tag{25}$$

where s denotes the curvilinear coordinate, c_{pl} denotes the specific heat of liquid water and $\eta < 1$ is the wet fraction of solid substrate. The boundary condition $T_l = T_s$, with T_s being the computed solid substrate temperature over the heated section, is imposed at $x = l_h$. Icing is triggered when the condition $T_l \leq 0\,^\circ\mathrm{C}$ is verified for the computed liquid temperature. When icing is detected, only still droplets are assumed to eventually freeze. The mean droplet age $\tau(r)$, evaluated via Equation (14), is compared with the freezing onset, set to $\tau_{ice} = 10^{-2}$ s: such a value is experimentally reported in [32] for icing experiments conducted on droplets on a cold surface under different conditions in terms of both surface wettability and environmental temperature. Still droplets with radius $r \leq r_{mov}$ so that $\tau(r) \geq \tau_{ice}$ are assumed to freeze instead of eventually grow due to coalescence. Since the shape of the accreting ice layer is beyond the scope of the present modeling approach, the validation is limited to the prediction of the eventual iced region.

According to [16], two different setups (named as setup 1 and setup 2) are investigated:

1. The whole airfoil surface is covered with the superhydrophobic coating, characterized by $\theta_s = 157^\circ$ (see Table 1);
2. The heated section is superhydrophilic with a static contact angle of $\theta_s = 15^\circ$, while the the superhydrophobic coating is applied elsewhere.

Here, a dropwise regime is assumed over the superhydrophobic domain, while a filmwise regime is assumed over the superhydrophilic region (where the PBM yields a wet fraction $\eta \geq 1$): if a dropwise regime is assumed, the PBM is applied to estimate the liquid flow rate and the evaporating mass flux; if a continuous liquid layer is assumed, a standard shear-driven film model is applied to estimate the liquid flow rate via Equation (23), while the evaporating mass flux is estimated via the heat and mass transfer analogy:

$$\dot{m}_{lv}'' = \mathrm{Sh}\, \frac{D_v}{l_c}\, \frac{p_{sat}(T_s) - \phi\, p_{sat}(T_\infty)}{R_v\, T_s} \tag{26}$$

Figure 7a shows the averaged liquid thickness solution along the heated section: when setup 1 is considered (i.e., the whole airfoil surface is superhydrophobic, yielding a dropwise regime) h, expressed by Equation (7), includes the contributions of both the stationary droplets (having $r \leq r_{mov}$) and the moving ones ($r > r_{mov}$); on the other hand, when setup 2 is considered (i.e., the heated section is superhydrophilic, yielding a continuous film regime), h represents the thickness of the moving liquid film. Figure 7b shows the liquid flux along the chordwise coordinate (given by the contributions of impinging and evaporation) for the superhydrophobic (setup 1) and superhydrophilic (setup 2) surfaces (the black, dashed line corresponds to the case with no active system, i.e., only the contribution from the impinging process). All the impinging liquid evaporates before leaving the heated section when it is covered with a superhydrophobic coating, meaning that a population of stationary droplets is observed at the end of the heated section and a dry surface is predicted immediately downstream, whereas a residual liquid flux leaving the heated section is observed for the superhydrophilic coating (resulting in a continuous film regime). Therefore, the evaporation rate predicted by the PBM is higher than that estimated via a standard Messinger model, valid for a continuous wetting layer, at the same specific heat flux imposed through the heated section. Consistently with the experimental evidence of [16], a dry surface is observed out of the heated section when the airfoil surface is fully superhydrophobic (setup 1), while a liquid flow rate exiting the heated section of length l_h is numerically observed when it is covered with a superhydrophilic coating (setup 2).

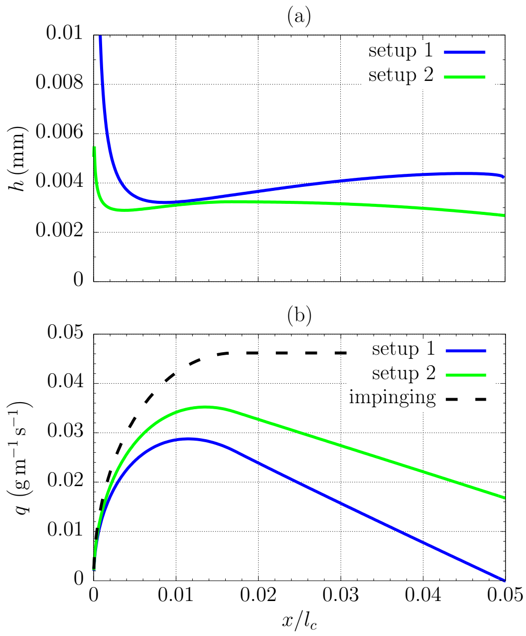

Figure 7. (**a**) Averaged liquid thickness along heated section: setup 1 (superhydrophobic) vs. setup 2 (superhydrophilic). (**b**) Computed liquid flux: setup 1 vs. setup 2. Dashed line depicts the liquid flux due solely to impinging process (i.e., evaporation is suppressed). $\dot{Q}_s'' = 13\,\mathrm{kW/m^2}$, $r_{imp} = 5\,\mu\mathrm{m}$, $l_c = 150\,\mathrm{mm}$, $LWC = 1\,\mathrm{g/m^3}$, $u_\infty = 40\,\mathrm{m/s}$.

Thus, Equation (25) is solved for $x > l_h$ to evaluate the liquid temperature. Since the substrate is superhydrophobic for $l_h < x < l_c$, the PBM predicts the transition from a continuous film (observed over the superhydrophilic heated section, $x \leq l_h$) to a dropwise regime. Figure 8b shows that icing is triggered at $x/l_c \simeq 0.18$, where the local liquid temperature is equal to 0 °C. Once the first beads form, they will create an obstacle and the ice accretion process (here not modeled) extends the iced area upstream. All stationary droplets having $r < r_{mov}$, characterized by $\tau(r) \geq \tau_{ice}$, freeze until the liquid flux vanishes at $x/l_c \simeq 0.26$. Comparison of the predicted iced region with the experimental observations of [16], shown in Figure 8a, shows good agreement, with both the location and the extent of the iced region being reasonably well predicted. Finally, it is worth pointing out that a standard Messinger model, which assumes a continuous film wetting the solid substrate, is not able to predict different behaviors for the two strategies (fully superhydrophobic surface and hybrid superhydrophilic/superhydrophobic surface), since the effect of surface wettability is not included. Indeed, Figure 8a shows that a standard Messinger model (green dashed line) does not provide an accurate estimate of the liquid temperature T_l over the airfoil surface and, thus, of the icing onset (corresponding to $T_l = 0$ °C) when a superhydrophobic surface is considered.

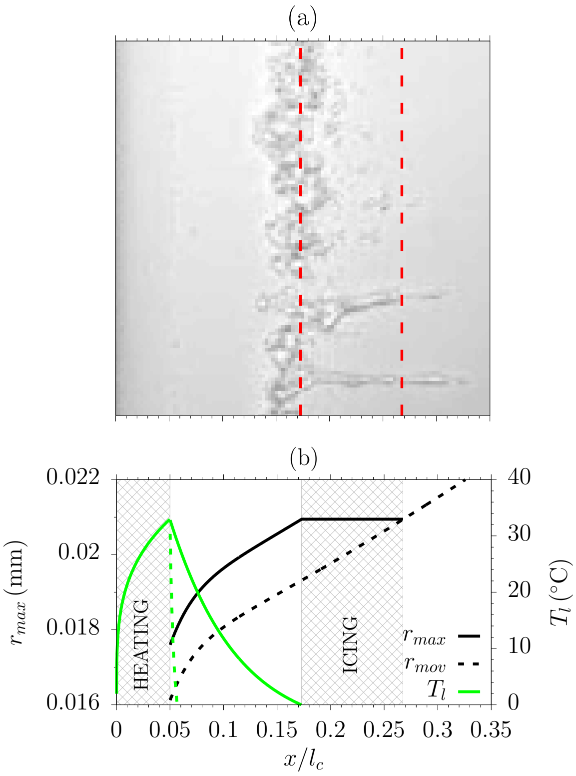

Figure 8. (**a**) Experimental observation of [16], setup 2 (superhydrophilic/superhydrophobic hybrid strategy with 5% of chord length heated); the iced region predicted by the PBM is emphasized with dotted lines. (**b**) Maximum droplet radius (black line, defined only for dropwise regime) and liquid temperature (green lines, solid for the PBM and dashed for a standard Messinger model) along the chordwise coordinate, setup 2.

4. Conclusions

A novel probability-based model (PBM) was developed to predict the evolution of a droplet population on a solid surface. The statistical information regarding the droplet size distribution was derived from numerical computations obtained using a high-fidelity individual-based model (IBM), which follows the history of each droplet at the cost of high computational effort. As mentioned in Section 3.1, IBM computations on a small patch of airfoil surface required hours on an 8-core workstation, in contrast to the nearly instantaneous response of the PBM model. Compared to the standard shear-driven film assumption, the present PBM includes the effect of the local liquid pattern (dropwise or filmwise) on the runback water flow and, when an active anti-icing system is used, on the mass transfer due to evaporation process. Furthermore, a criterion to predict the onset of icing is presented for the case of passive anti-icing systems operating in a dropwise regime. These aspects are crucial to evaluate the influence of substrate wettability in the design of both passive anti-icing systems (via superhydrophobic and ice-phobic surfaces) and active anti-icing systems, filling the gap of previous Messinger-like models. The PBM model was validated with experimental observations from the literature [16] for a setup correlated to in-flight ice applications, showing its capability to model how the surface wettability affects the local liquid pattern and to predict the onset of icing. Thus, the presented PBM can be integrated with a CFD simulation of the air flow past an aircraft and with a proper ice accretion model to predict the ice growth on the aircraft surface.

Results show that the rough prediction of the liquid flow pattern (dropwise or filmwise) and of the possible transitions based on the wet fraction is reasonable for the investigated test case. However, the model will be extended to include a transitional rivulet regime, following the approach proposed in [4,33]. The heat transfer model will be also refined, adding the thermal resistance correlated to conduction through the liquid droplet core [19] and implementing the size distribution of the small drop ($r < r_0$) population to evaluate the latent heat flux contribution from smaller droplets. Furthermore, a dedicated model will be addressed to predict the freezing of supercooled droplets on a solid surface.

Author Contributions: Conceptualization, G.C. and N.S.; methodology, G.C. and N.S.; software, N.S.; validation, N.S.; formal analysis, G.C. and N.S.; investigation, N.S.; resources, G.C.; data curation, N.S.; writing—original draft preparation, G.C. and N.S.; writing—review and editing, G.C. and N.S.; visualization, G.C. and N.S.; supervision, G.C. All authors have read and agreed to the published version of the manuscript.

Funding: This research received no external funding.

Institutional Review Board Statement: Not applicable.

Informed Consent Statement: Not applicable.

Data Availability Statement: The data presented in this study are available on request from the corresponding author.

Conflicts of Interest: The authors declare no conflicts of interest.

Abbreviations

The following abbreviations are used in this manuscript:

IBM	individual based model
PBM	probability-based model

References

1. Shinan, C.; Liang, D.; Mengjie, S.; Mengyao, L. Numerical investigation on impingement dynamics and freezing performance of micrometer-sized water droplet on dry flat surface in supercooled environment. *Int. J. Multiph. Flow* **2019**, *118*, 150–164. [CrossRef]
2. Elliott, J.; Smith, F. Ice formation on a smooth or rough cold surface due to the impact of a supercooled water droplet. *J. Eng. Math.* **2017**, *102*, 35–64. [CrossRef]
3. Bourgault, Y.; Boutanios, Z.; Habashi, W. Three-dimensional Eulerian approach to droplet impingement simulation using FENSAP-ICE, Part 1: Model, al-gorithm, and validation. *J. Aircr.* **2000**, *37*, 95–103. [CrossRef]
4. Croce, G.; Suzzi, N.; Pretto, M.; Giannattasio, P. Numerical Modelling of Droplets and Beads Behavior over Super-Hydrophobic and Hydrophilic Coatings under in-Flight Icing Conditions. *Appl. Sci.* **2022**, *12*, 7654. [CrossRef]
5. Xu, Z.; Zeng, X.; Yang, S.; Yang, J. Numerical simulation of droplet impingement and film flow for three-dimensional wings. *Aeronaut. J.* **2024**, *128*, 1302–1322. [CrossRef]
6. Šikalo, Š.; Marengo, M.; Tropea, C.; Ganić, E. Analysis of impact of droplets on horizontal surfaces. *Exp. Therm. Fluid Sci.* **2002**, *25*, 503–510. [CrossRef]
7. Caviezel, D.; Narayanan, C.; Lakehal, D. Adherence and bouncing of liquid droplets impacting on dry surfaces. *Microfluid. Nanofluidics* **2008**, *5*, 469–478. [CrossRef]
8. Bourgault, Y.; Beaugendre, H.; Habashi, W. Development of a shallow-water icing model in FENSAP-ICE. *J. Aircr.* **2000**, *37*, 640–646. [CrossRef]
9. Croce, G.; De Candido, E.; Habashi, W.; Munzar, J.; Aubé, M.; Baruzzi, G.; Aliaga, C. FENSAP-ICE: Analytical Model for Spatial and Temporal Evolution of In-Flight Icing Roughness. *J. Aircr.* **2010**, *47*, 1283–1289. [CrossRef]
10. Ozcer, I.; Moula, G.; Page, J.; Zanon, A.; De Gennaro, M. Neubauer, T.; Schweighart, S.; Llamas-Sandin, R. IMPACT: Experimental and Numerical Ice Shapes on Swept-Wing Models with Straight and Undulated Leading Edges. In *Proceedings of the AIAA Aviation Forum and Ascend 2024, Las Vegas, NV, USA, 29 July–2 August 2024* ; American Institute of Aeronautics and Astronautics: Reston, VA, USA, 2024; p. 4160 . [CrossRef]
11. Messinger, B. Equilibrium temperature of an unheated icing surface as a function of air speed. *J. Aeronaut. Sci.* **1953**, *20*, 29–42. [CrossRef]
12. Myers, T. Extension to the Messinger Model for Aircraft Icing. *AIAA J.* **2001**, *39*, 211–218. [CrossRef]
13. Ahmed, H.; Shad, A.; Zgheib, N.; Sherif, S.; Balachandar, S. A rigorous framework for an improved Messinger/Myers modelof ice accretion under conditions of variable property and unsteady aircraft icing. *Philos. Trans. R. Soc. A* **2025**, *383*, 20240367. [CrossRef]

14. Zheng, S.; Li, C.; Fu, Q.; Hu, W.; Xiang, T.; Wang, Q.; Du, M.; Liu, X.; Chen, Z. Development of stable superhydrophobic coatingson aluminum surface for corrosion-resistant, self-cleaning, and anti-icing applications. *Mater. Des.* **2016**, *93*, 261–270. [CrossRef]
15. Liu, Y.; Hu, H. Experimental investigation on Bio-inspired Icephobic Coatings for Aircraft Inflight Icing Mitigation. In *Ice Adhesion: Mechanism, Measurement and Mitigation*; Mittal, K., Choi, C.H., Eds.; Wiley: Hoboken, NJ, USA , 2020. [CrossRef]
16. Hu, H.; Hu, H.; Liu, Y. An Explorative Study to Use Super-Hydrophilic/Super-Hydrophobic Hybrid Surfaces for Aircraft Icing Mitigation. In *SAE Technical Paper 2019-01-1995*; Society of Automotive Engineers International: Warrendale, PA, USA , 2019. [CrossRef]
17. Esmaeilifar, E.; Jung, K.; Myong, R. Computational simulation of in-flight ice accretion on superhydrophobic surfaces of airfoils considering wettability effects. *Aerosp. Sci. Technol.* **2026**, *178*, 112431. [CrossRef]
18. Li, A.; Xu, Y.; Qiu, C.; Pang, J.; Xu, Z.; He, Q. Dynamic de-icing mechanism analysis of propeller superhydrophobic surface droplets in flight environment. *Aerosp. Sci. Technol.* **2026**, *168*, 110908. [CrossRef]
19. Suzzi, N.; Croce, G. High fidelity and simplified modeling of evaporation over hydrophobic surfaces for anti-icing applications. *Int. J. Numer. Methods Heat Fluid Flow* **2026**, *ahead-of-print*. [CrossRef]
20. Kim, H.Y.; Lee, H.; Kang, B. Sliding of Liquid Drops Down an Inclined Solid Surface. *J. Colloid Interface Sci.* **2002**, *247*, 372–380. [CrossRef] [PubMed]
21. El Sherbini, A.; Jacobi, A. Retention forces and contact angles for critical liquid drops on non-horizontal surfaces. *J. Colloid Interface Sci.* **2006**, *299*, 841–849. [CrossRef]
22. Hu, H.; Larson, R. Evaporation of a sessile droplet on a substrate. *J. Phys. Chem. B* **2002**, *106*, 1334–1344. [CrossRef]
23. Castillo, J.; Weibel, J. A point sink superposition method for predicting droplet interaction effects during vapor-diffusion-driven dropwise condensation in humid air. *Int. J. Heat Mass Transf.* **2018**, *118*, 708–719. [CrossRef]
24. Aldhaleai, A.; Khan, F.; Thundat, T.; Tsai, P. Evaporation dynamics of water droplets on superhydropho-bic nanograss surfaces. *Int. J. Heat Mass Transf.* **2020**, *160*, 120149. [CrossRef]
25. Kim, S.; Kim, K. Dropwise Condensation Modeling Suitable for Superhydrophobic Surfaces. *J. Heat Transf.* **2011**, *133*, 081502. [CrossRef]
26. Liu, X.; Cheng, P. Dropwise condensation theory revisited: Part I. Droplet nucleation radius. *Int. J. Heat Mass Transf.* **2015**, *83*, 833–841. [CrossRef]
27. Liu, X.; Cheng, P. Dropwise condensation theory revisited Part II. Droplet nucleation density and condensation heat flux. *Int. J. Heat Mass Transf.* **2015**, *83*, 842–849. [CrossRef]
28. Le Fevre, E.; Rose, J. A theory of heat transfer by dropwise condensation. In *Proceedings of the 3rd International Heat Transfer Conference, Chicago, IL, USA, 7–12 August 1966*; American Institute of Chemical Engineers: New York, NY, USA, 1966; pp. 362–375.
29. Zheng, S.; Eimann, F.; Philipp, C.; Fieback, T.; Gross, U. Experimental and modeling investigations of dropwise condensation out of convective humid air flow. *Int. J. Heat Mass Transf.* **2020**, *151*, 119349. [CrossRef]
30. Gao, L.; Liu, Y.; Ma, L.; Hu, H. A hybrid strategy combining minimized leading-edge electric-heating and superhydro-/ice-phobic surface coating for wind turbine icing mitigation. *Renew. Energy* **2019**, *140*, 943–956. [CrossRef]
31. Clift, R.; Grace, J.; Weber, M. *Bubbles, Drops, and Particles*; Academic Press: New York, NY, USA; London, UK, 1978.
32. Guo, C.; Zhang, M.; Hu, J. Icing delay of sessile water droplets on superhydrophobic titanium alloy surfaces. *Colloids Surfaces A Physicochem. Eng. Asp.* **2021**, *621*, 126587. [CrossRef]
33. Wang, F.; Cheng, X. Modeling approach of flowing condensate coverage rate on inclined wall for aerosol wash down. *Nucl. Eng. Des.* **2019**, *355*, 110349. [CrossRef]